ATLAS CONF Note

ATLAS-CONF-2017-074

20th September 2017

Measurement of the fragmentation function for photon-tagged jets in $\sqrt{s_{\mathrm{NN}}} = 5.02$ TeV Pb+Pb and pp collisions with the ATLAS detector

The ATLAS Collaboration

This note presents a measurement of the charged-particle fragmentation function (FF) for jets azimuthally balanced by a high transverse momentum (p_{T}) prompt, isolated photon. FFs as a function of particle-p_{T} and fraction of the jet p_{T} carried by the particle, z, are measured in 26 pb^{-1} of pp and 0.49 nb^{-1} of Pb+Pb collision data at $\sqrt{s_{\mathrm{NN}}} = 5.02$ TeV recorded with the ATLAS detector at the Large Hadron Collider. In pp collisions, a comparison of the photon-tagged jet FF to that for inclusively selected jets is sensitive to the difference in fragmentation between quark– and gluon–initiated jets in vacuum. The ratio of the FF in Pb+Pb events to those in pp events with the same selection on the photon kinematic variables provides information on the modification of the parton shower for quark-initiated jets as they traverse the hot nuclear medium. In comparison to the modified FF for inclusively-selected jets, photon-tagged jets show a similar modification in particle-p_{T} or z in semi-central and peripheral events, but a stronger one in central events.

ATLAS-CONF-2017-074
25 September 2017

1 Introduction

A characteristic phenomenon associated with the formation of a hot nuclear medium in ultrarelativistic nucleus–nucleus collisions is jet quenching, the attenuation and distortion of the parton shower from high transverse momentum (p_{T}) jets as they traverse the medium. At the Large Hadron Collider (LHC), jet quenching manifests itself experimentally through the modification of several observables in lead–lead (Pb+Pb) collisions compared to that in proton–proton (pp) collisions. These include the suppression of inclusive jet and hadron production rates [1, 2], and the distortion of the p_{T} balance of di-jet pairs from that in vacuum [3, 4].

In addition to an overall transport of momentum to large angles relative to the initial parton direction [5, 6], the medium also modifies the internal structure of the shower which remains correlated with the initial parton direction. Previous measurements of the jet fragmentation function (FF) for inclusively produced jets [7, 8] show that these modifications are modest but have a characteristic dependence on the fragment p_{T}. However, the jets in Pb+Pb collisions are selected via their final-state p_{T} after quenching effects, whose flavor composition and initial hard scattering p_{T} may be different than those selected in pp collisions. Therefore, the selected jets in Pb+Pb collisions may be biased towards those which have suffered only modest modifications, complicating interpretations of the data [9, 10]. Alternatively, the jet flavor and initial hard scattering p_{T} can be tagged via the presence of an associated particle unmodified by the presence of the hot nuclear medium, e.g. a photon or Z boson [11–13].

This note presents a measurement of the jet FF for high-p_{T} jets azimuthally balanced with a prompt, isolated photon in pp and Pb+Pb collisions at a center of mass energy of 5.02 TeV per nucleon pair, made using the ATLAS detector. A measurement of the jet FF in this experimental channel is newly possible due to the large integrated luminosity in LHC Run 2. The measurement in this note is corrected for detector effects, allowing for a direct comparison with models, and also provides complementary information to the FF previously measured for inclusive jets [14, 15]. Events are selected via the final-state signature of the high-p_{T} photon, which is unaffected by its passage through the nuclear medium [16]. Thus, there is no a posteriori bias imposed on the jet sample, and it is possible to select common distributions of parton kinematics before quenching in the hot, dense medium is initiated. Additionally, the jets created in coincidence with prompt photons are likely to be initiated by the showering of quarks, providing a handle on how energy loss depends on the flavor of the initiating parton (in this case, predominantly light quarks). Finally, the presence of the photon substantially reduces the relative rate of jets reconstructed from UE fluctuations on its away side, allowing for a measurement of jet structure down to lower p_{T} which is challenging for inclusive jets.

Previous photon+jet results have taken advantage of the information from the photon to provide complementary insights to other jet and hadron measurements. Analysis of the photon–hadron p_{T} correlations in nucleus–nucleus collisions at the Relativistic Heavy Ion Collider were aimed at exploiting the benefits described above [17, 18]. At the LHC, preliminary measurements of the medium-induced p_{T} imbalance of photon+jet pairs [11, 12] have inspired much theoretical interest [19–21]. The measurement presented here complements these analyses by exploring the FF of the jets recoiling against a photon. These two measurements, the p_{T} imbalance between the photon and recoil jet and the fragmentation of the recoil jet, can together disentangle the overall energy loss from the modification of the fragmentation pattern, probing for example color coherence effects [22].

As utilized in previous inclusive jet analyses, the per-jet charged particle FFs for a jet to contain a fragment with a given p_{T} are defined as

$$D(p_{\mathrm{T}}) = \frac{1}{N_{\mathrm{jet}}} \frac{\Delta N(p_{\mathrm{T}})}{\Delta p_{\mathrm{T}}} \tag{1}$$

$$D(z) = \frac{1}{N_{\mathrm{jet}}} \frac{\Delta N(z)}{\Delta z} \tag{2}$$

where the longitudinal momentum fraction z is defined as $p_{\mathrm{T}} \cos \Delta R / p_{\mathrm{T}}^{\mathrm{jet}}$, $\Delta R = \sqrt{(\eta^{\mathrm{jet}} - \eta)^2 + (\phi^{\mathrm{jet}} - \phi)^2}$ [1], and only charged particles within $\Delta R < 0.4$ are considered.

2 Experimental setup, reconstruction and data selection

The ATLAS detector [23] is a multi-purpose detector with a forward-backward symmetric cylindrical geometry. For this measurement, its relevant components include an inner tracking detector surrounded by a thin superconducting solenoid, electromagnetic and hadronic calorimeters, and a high-level online trigger system. The inner-detector system is immersed in a 2 T axial magnetic field and provides charged-particle tracking in the range $|\eta| < 2.5$. In order of closest to furthest from the beam pipe, it consists of a high-granularity silicon pixel detector which provides four measurements per track and a silicon microstrip tracker which typically provides four three-dimensional space point measurements per track. These silicon detectors are complemented by the transition radiation tracker, which enables radially extended track reconstruction up to $|\eta| = 2.0$. The calorimeter system covers the range $|\eta| < 4.9$. In the region $|\eta| < 3.2$, electromagnetic calorimetry is provided by barrel and endcap high-granularity lead/liquid-argon (LAr) electromagnetic calorimeters, with an additional thin LAr presampler covering $|\eta| < 1.8$ to correct for energy loss in material upstream of the calorimeters. Within the region of the measurement, the LAr calorimeters are divided into three layers in depth. Hadronic calorimetry is provided by a steel/scintillator-tile calorimeter, segmented into three barrel structures within $|\eta| < 1.7$, and two copper/LAr hadronic endcap calorimeters, which cover the region $1.5 < |\eta| < 3.2$. The solid angle coverage is extended out to $|\eta| = 4.9$ with a forward calorimeter (FCal) composed of copper/LAr and tungsten/LAr modules optimised for electromagnetic and hadronic measurements, respectively. Finally, zero-degree calorimeters (ZDC) are situated at far pseudorapidity, $|\eta| > 8.3$, and are primarily sensitive to spectator neutrons.

During data-taking, events are initially selected using a first-level trigger based on energy deposition in the electromagnetic calorimeter implemented in custom electronics. Software algorithms with access to the full detector information, including an estimate of the underlying event (UE) contribution to the E_{T} measured in the calorimeter in Pb+Pb collisions [16], are then used in the high-level trigger [24] to select events consistent with a high transverse momentum (E_{T}^{γ}) photon candidate.

Photons are reconstructed following a procedure used for previous measurements of isolated prompt photon production in Pb+Pb collisions [16]. It is similar to that used extensively in pp collisions [25, 26], but is applied to the set of calorimeter cells after an event-by-event estimation and subtraction of

[1] ATLAS uses a right-handed coordinate system with its origin at the nominal interaction point (IP) in the centre of the detector and the z-axis along the beam pipe. The x-axis points from the IP to the centre of the LHC ring, and the y-axis points upward. Cylindrical coordinates (r, ϕ) are used in the transverse plane, ϕ being the azimuthal angle around the z-axis. The pseudorapidity is defined in terms of the polar angle θ as $\eta = -\ln \tan(\theta/2)$. Transverse momentum and transverse energy are defined as $p_{\mathrm{T}} = p \sin\theta$ and $E_{\mathrm{T}} = E \sin\theta$, respectively. ΔR is defined as $\sqrt{(\Delta\eta)^2 + (\Delta\phi)^2}$.

the pile-up and UE contribution to the deposited energy in each cell [5]. Photon candidates are initally reconstructed from clusters of energy deposited in the electromagnetic calorimeter. Their identification is based primarily on detailed shower shapes in the calorimeter [27], selecting those which are compatible with that originating from a single photon impacting the calorimeter. The measurement of the photon energy is based on the energy collected in the core set of calorimeter cells ($\Delta\eta \times \Delta\phi = 0.075 \times 0.175$ in the barrel and $\Delta\eta \times \Delta\phi = 0.125 \times 0.125$ in the end-caps), and is corrected via a dedicated calibration [28] which accounts for upstream losses and both lateral and longitudinal leakage. The transverse energy sum of calorimeter cells inside a cone size of $R = 0.3$ centered on the photon, excluding a small area of size $\Delta\eta \times \Delta\phi = 0.125 \times 0.175$ centered on the photon, is used to compute the isolation energy $E_{\mathrm{T}}^{\mathrm{iso}}$. It is corrected for the expected leakage of the photon energy from outside this region into the isolation cone.

Jets are reconstructed following the procedure used previously by ATLAS for jet measurements in pp and Pb+Pb collisions [1, 5, 29], which is briefly summarized here. The anti-k_t algorithm [30] with $R = 0.4$ is applied to energy deposits in the calorimeter grouped into towers of size $\Delta\eta \times \Delta\phi = 0.1 \times 0.1$. An iterative procedure is used to obtain an event-by-event estimate of the average η-dependent UE energy density, while excluding jets from that estimate. An updated estimate of the jet four-momentum is obtained by subtracting the UE energy from the constituent towers of the jet. This procedure is also applied to pp collisions, for which the UE subtraction removes the small energy density deposited from additional collisions in the same bunch crossing. The p_{T} of the resulting jets is corrected for the calorimeter energy response using an η- and p_{T}-dependent calibration derived from simulation. Additional corrections derived from *in situ* studies of events with a jet recoiling against a photon or Z boson, and from the differences between the heavy-ion reconstruction algorithm and that normally used in the 13 TeV data [31], are applied. A final correction at the analysis level is applied to correct for a non-closure in the mean p_{T} response arising from a different jet flavor composition in the event sample compared to that used to derive the calibration [11].

Charged-particle tracks are reconstructed from hits in the inner detector using an algorithm optimized for the large occupancy in heavy ion collisions [2, 8]. Tracks used in this analysis are required to have a minimum number of hits in the silicon pixel and microstrip detectors together, corresponding to hits in at least 9 (11) layers for $|\eta| < 1.65$ ($|\eta| > 1.65$), with at least one hit in one of the two innermost layers. Along the projection of the reconstructed track, the track is required to have a hit at the point where the projection intersects with the innermost layer, and may not miss more than two such expected hits in the outer layers. Additionally, to suppress the rate of tracks from secondary particles, the distance of closest approach of the track to the primary vertex is required to be smaller than 1.0 mm in the longitudinal direction and smaller than a p_{T}-dependent value which varies from 0.45–0.20 mm in the transverse plane.

Photon+jet events in Pb+Pb and pp collisions are initially selected for analysis by the high-level triggers described above. Events are required to have the calorimeters, tracking detectors and data acquisition system in nominal operation, and to contain a reconstructed vertex in the inner detector. Pb+Pb events which are consistent with the presence of two hadronic Pb+Pb interactions are identified via the correlation of the signals in the ZDC and forward calorimeters and are rejected. Two classes of Pb+Pb events are defined based on the total transverse energy measured in the FCal, $\sum E_{\mathrm{T}}$. Central events are defined as those with the top 30% (0–30%) of the measured $\sum E_{\mathrm{T}}$ values among hadronic Pb+Pb events, which have a large nuclear overlap and thus a larger, hotter, longer-lived nuclear medium. Peripheral events are defined as those with a $\sum E_{\mathrm{T}}$ value in the 30–80% centile range, and have a somewhat smaller nuclear overlap region. The mean number of nucleon–nucleon collisions is 1081 and 135, respectively, in these selections.

3 Monte Carlo simulation and fiducial definition

Monte Carlo (MC) simulations of photon+jet events are used to study the performance of the ATLAS detector for the measurement and provide generator-level calculations which incorporate a full parton shower for comparison to data.

For the primary simulation sample, the Pythia 8.186 [32] generator was used with the NNPDF23LO parton distribution function set [33], and a set of generator parameters tuned to reproduce a set of minimum bias data ("A14" tune) [34]. In the simulation, both the direct and fragmentation photon contributions are included to produce events with a generator-level photon in the p_{T} range 70 to 140 GeV. Events are passed through a full Geant4 simulation of the ATLAS detector [35, 36], and are digitized and reconstructed in the same way as the data. Two million pp events are generated in this way. Additionally, a sample of eight million events are generated which are overlaid with minimum bias Pb+Pb events. The simulated Pb+Pb events are reweighted on an event-by-event level to match the $\sum E_{\mathrm{T}}$ distribution observed in the events in data selected for analysis. Thus, the Pb+Pb event sample contains the effects of the UE identical to that observed in data. Additionally, the distributions in MC which are sensitive to jet quenching, such as the jet p_{T} distribution, are weighted to match those measured in data.

Additional samples of 10^5 and 2×10^6 pp and Pb+Pb events, respectively, are produced with the Sherpa 2.1.1 [37] generator using the CT10 parton distribution functions [38]. These samples were generated with leading order matrix elements for photon-plus-jet final states with up to three additional partons, which were merged with the Sherpa parton shower. Additionally, 2×10^5 Herwig 7 [39] events with the MMHT UE tune and PDF set [40] were generated in a way which includes the direct and fragmentation photon contributions. Both Sherpa and Herwig samples were filtered on the presence of a photon in the required kinematic range, and are used because they contain a different description of photon+multijet topologies and of the jet flavor composition.

At the generator level, photons are required to be isolated according to the sum of the transverse energy carried by final-state particles in a $R = 0.3$ cone around the photon, $E_{\mathrm{T}}^{\mathrm{iso}}$, to be smaller than 3 GeV. Primary particles are defined as those with a proper mean lifetime, τ, exceeding $c\tau = 10$ mm which are either directly produced in pp interactions or from the subsequent decays of shorter-lived paticles. All other particles are considered to be secondary. Jets are defined by applying the anti-k_t algorithm with $R = 0.4$ to stable particles, excluding muons and neutrinos. The jet flavor (whether it is quark– or gluon–initiated) is defined by association with the highest-p_{T} parton nearest to the jet in ΔR [41].

The analysis selects events with a prompt, isolated photon with E_{T}^{γ} in the range 79.6 GeV to 126 GeV and absolute pseudorapidity smaller than 2.37, excluding the region $1.37 < |\eta^{\gamma}| < 1.56$. In these events, the fiducial jet selection corresponds to the jets which are azimuthally balanced with the photon according to $|\Delta\phi| > 7\pi/8$ and have $63.1 < p_{\mathrm{T}}^{\mathrm{jet}} < 144$ GeV and $\left|\eta^{\mathrm{jet}}\right| < 2.1$. This jet p_{T} range is chosen to enhance the contribution from topologies with a single high-p_{T} balancing jet over that from multiple low-p_{T} jets [42]. Specifically, the minimum jet p_{T} is equal to half the maximum photon p_{T}, meaning that events with two jets balancing the photon are kinematically suppressed. Charged particles with $p_{\mathrm{T}} > 1$ GeV within an $R = 0.4$ of the jet cone are included in the definition of the FF.

The upper panel of Figure 1 compares the p_{T} distribution of jets passing the given $\Delta\phi$ and η requirements in generator-level Pythia, Sherpa and Herwig events with a high-p_{T} photon, separately for just the highest-p_{T} jet and for all jets which meet the requirements. It can be seen that in the jet p_{T} selection considered in this analysis, only leading jets are selected. The bottom panel of Figure 1 shows the quark

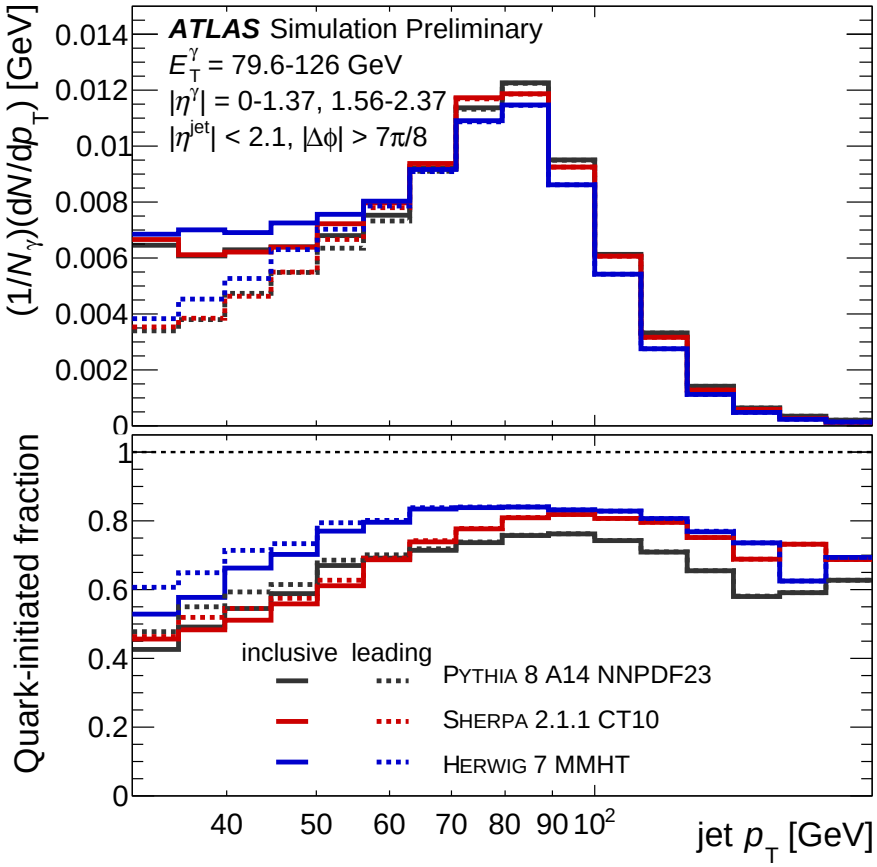

Figure 1: *Top:* p_T distribution for jets passing the fiducial selection in generator events, comparing the distribution for all jets in the fiducial selection and for only the leading jet. *Bottom:* Fraction of jets initiated by a quark, for jets which pass the fiducial selection in generator events.

fraction as a function of jet p_T for the inclusive selection, demonstrating that the kinematic range of the measurement is dominated by a highly quark-enhanced sample.

In the measurement, jets and charged particles are initially reconstructed in a larger kinematic range than the selection indicated above, to allow for the correction of bin migration in jet and particle p_T across the fiducial region boundaries.

4 Data analysis and corrections

The measurement of the per-jet FF has two principal components which are constructed and corrected separately and then combined: the measurement of the total associated jet yield in photon-containing events, and the measurement of the total charged particle yield in this set of associated jets. This approach has been used in previous measurements of the jet FF [8, 14] and is needed to account for the simultaneous bin migration in the jet and charged particle kinematic variables, as well as accounting for correlations in the calorimeter response and fragmentation patterns of jets. The jet and charged particle yields are

first corrected for backgrounds through data-driven techniques, and then corrected for the effects of bin migration.

Photon+jet events are initially selected for analysis by requiring the presence of a photon in the desired kinematic range which passes a strict set of identification requirements and is experimentally isolated via $E_{\mathrm{T}}^{\mathrm{iso}} < 3$ GeV (< 10 GeV) in pp (Pb+Pb) collisions. Simulation studies show that the combined reconstruction, identification and selection efficiencies are 90%, 85% and 65–70% in pp, peripheral and central Pb+Pb events, respectively. This initial selection contains an admixture of hadrons and non-isolated fragmentation photons, and therefore the contribution to the measurement from the jets in these events must be accounted for. The purity of the selected photon sample is determined via the standard double sideband ("ABCD") approach extensively used in photon production measurements in ATLAS [25, 26]. In this method, the identification and isolation requirements are inverted to select background enhanced samples of photons, the relative yields of which are used to estimate the background contribution to the isolated and identified set of candidate photons. The resulting purity is 94%, 80% and 83% in pp, peripheral and central collisions, respectively.

4.1 Jet yield measurement

The yield of photon-associated jets is determined by measuring the p_{T} distribution for all jets azimuthally balanced with a high-p_{T} photon and correcting this estimate for two backgrounds. First, the combinatoric association rate of a photon in a Pb+Pb event with an unrelated jet, either from another hard scattering or a local UE fluctuation, is evaluated in the data overlay simulation. The yield in data is corrected for this per-photon rate. Second, the contribution of jets azimuthally balanced with misidentified neutral hadrons is estimated through an extension ot the sideband approach above which determines the purity. The jet yield azimuthally balanced with photons which are isolated but pass the background-enhancing inverted identification requirements is used as the background template, since this selection is strongly background dominated. This yield, normalized per background photon, is scaled to match the impurity determined in data and subtracted from the total yield.

Next, the background-subtracted yield must be corrected for the effects of bin migration and the total yield N_{jet} extracted. A study of the jet p_{T} response in simulation shows that after the full calibration sequence, the mean response is within 1% of unity, while the resolution at $p_{\mathrm{T}} = 63.1$ GeV is 21% in central events, 12% in pp events, and decreases systematically with increasing jet p_{T}. Since the jet p_{T} distribution is peaked within the p_{T} range over which the total yield is integrated, typically 90% of the jets with generator-level p_{T} in this range remain in the p_{T} range at the reconstructed-level. The correction to the yield is determined by comparing the total yield when the jet p_{T} is evaluated at the reconstructed level compared to the generator level in simulation, after reweighting the simulated p_{T} distribution to match that in data. The resulting correction to the yield is applied as a multiplicative correction factor and is smaller than 5%.

4.2 Charged particle yield measurement

The raw charged particle yield in photon-associated jets is initially determined by measuring the two-dimensional $(p_{\mathrm{T}}^{\mathrm{jet}}, p_{\mathrm{T}})$ or $(p_{\mathrm{T}}^{\mathrm{jet}}, z)$ distribution for all particles inside reconstructed jets azimuthally balanced with a high-p_{T} photon. Each charged particle is weighted by the inverse of the reconstrution efficiency evaluated at its p_{T} and η, which varies from 60% in Pb+Pb events at large rapidity to 80% or higher for

pp events at mid-rapidity. The efficiency-corrected yields are further corrected for three backgrounds: first, the contribution of UE particles and fake or secondary tracks are estimated by examining the p_{T} distributions of tracks inside jets which are not matched to a truth particle in the simulation. Since they correspond to particles inside combinatorial photon+jet pairs, they are subtracted statistically from the yields on a per-photon basis. Second, the contribution to the yield from charged particles in jets not correlated with the photon is estimated and subtracted on a per-photon basis as above. Third, the contribution from the charged particle yield in jets azimuthally balanced with a background photon is determined via the sideband approach, scaled to match the impurity in the photon selection, and statistically subtracted, as above.

The two-dimensional yield is corrected for the bin migration, arising from the finite detector resolution, along both axes via a Bayesian unfolding procedure [43, 44]. Before the unfolding, the distributions in simulation are reweighted to match those in data. The unfolding is performed with a varying number of iterations, calculating the total statistical uncertainty on the unfolded result, and the sum of squares of the differences between the unfolded result with and without the reweighting. The choice for the nominal number of iterations is chosen by minimizing this quadrature sum. After unfolding, the total charged particle yield is determined by projecting the two-dimensional distribution within the jet p_{T} range corresponding to the fiducial analysis selection. The change in the yield induced by the unfolding procedure is typically only 5 in *pp* collisions and up to 10% in Pb+Pb collisions, with the small size of the correction resulting primarily from the wide kinematic bins used in the measurement relative to the experimental resolution.

This procedure is tested by dividing the MC events into statistically independent halves, and using the response determined in one half to unfold the measured distribution in the other half. The original generator-level distributions are recovered by the unfolding within statistical uncertainties.

5 Systematic uncertainties

The primary sources of systematic uncertainties affecting the measurement are investigated. These include uncertainties related to the jet p_{T} measurement, the photon purity, the charged-particle selection and p_{T} measurement, and those related to the unfolding and physics modeling. Some systematic variations, such as the jet- and photon–related ones, typically caused the jet and charged particle yield to change in a significant but highly correlated way, with the result that the per-jet normalized FFs had a much smaller sensitivity than either quantity alone. Additionally, most uncertainty sources are treated as correlated between the *pp* and Pb+Pb systems, resulting in a partial cancellation when they are evaluated for the ratios of FFs.

The measurement is affected by uncertainties related to the jet energy scale and resolution. These include: the baseline uncertainties in the energy scale and resolution common to jet measurements in ATLAS [31, 41]; an additional uncertainty determined through differences between the heavy ion style jet reconstruction used here and that used in analyses of 13 TeV *pp* data [45]; an uncertainty in the flavor composition and the flavor-dependent jet response [46], evaluated specifically for the photon+jet sample; an additional energy scale uncertainty for jets in heavy ion collisions, evaluated via *in situ* track-to-calo jet energy comparisons in data and simulation.

The measurement is sensitive to uncertainties which affect the photon purity estimate. This sensitivity is quantitatively tested through three variations used in the analysis: the inverted identification criteria used

to select hadron background candidates are loosened and tightened, resulting in a different background estimate; the inverted isolation criteria used to select the non-isolated background are tightened, resulting in a different background estimate; a possible non-factorization of the hadron background along the isolation and identification axes is considered.

The measurement is susceptible to uncertainties which arise in the charged particle reconstruction, selection, and efficiency determination, and are described in detail in Refs. [8, 47]. This is evaluated in several ways: the track selection is made more stringent by requiring a tighter compatibility of the transverse and longitudinal impact parameters with the primary vertex; an uncertainty on the measured momentum of the track is evaluated; at the generator-level, the truth association requirement is made more stringent, resulting in a higher estimated fake rate but a compensating lower efficiency; an uncertainty on the efficiency associated with tracking in the dense jet core is based on the studies in Ref. [48]; an uncertainty on the efficiency associated with the description of inactive material in the simulation is evaluated; and the uncertainty on the fake-track rate in simulation is included.

Finally, the sensitivity of the measurement to three unfolding and physics modeling sources is determined in the following ways: the effect of limitations in the MC statistics is evaluated through a toy re-sampling of the response matrices; the sensitivity of the unfolded result to the prior distributions is evaluated by repeating the unfolding without the reweighting of the jet p_{T} distribution; instead of Pythia 8, the analysis is repeated but using Sherpa pp and Pb+Pb events as the main simulation samples.

The total uncertainty on the $D(z)$ and $D(p_{\mathrm{T}})$ distributions and their ratios are typically 5% at moderate z or p_{T} values and multiple uncertinaties are of similar magnitude. At low p_{T} or z, the uncertainty related to the track selection rises sharply. In Pb+Pb collisions, this uncertainty is as large as 30% due to the challenging nature of charged-particle tracking in the dense environment. At large p_{T} or z, where the FF is very steeply falling, the uncertainties related to the shape of the prior distribution and the choice of physics model become dominant and are as large as 20%.

6 Results

Figure 2 shows the corrected $D(p_{\mathrm{T}})$ and $D(z)$ distributions for jets azimuthally balanced with a high-p_{T} photon in pp and Pb+Pb events. The measured values span three orders of magnitude over the measured kinematic range, which spans over nearly two orders of magnitude in z or p_{T}.

Figure 3 shows a comparison of the distributions in pp collisions to the generator-level distribution in Pythia 8, and to the FFs for inclusive jets measured in pp collisions at the same collision energy and in a similar jet p_{T} range [8]. The Pythia 8 model, configured with parameters according to the A14 tune and using the NNPDF23LO PDF set, successfully describes the data within its uncertainties at low to moderate values of z and p_{T}. However the central value of this model over-predicts the data at higher values. The FF for photon-tagged jets is systematically harder than that for inclusive jets at similar p_{T}, a feature which arises from the different flavor composition of the two samples. This observation is consistent with the expectations from, for example, LEP data [49–51] that the FFs for quark-initiated jets are harder than those for gluon-initiated ones.

Figure 4 shows the ratio of the photon-tagged FFs in Pb+Pb collisions to those in pp collisions. In peripheral collisions, the modifications are characterized by an excess at low z or p_{T}, a depletion at moderate z and p_{T}, and an enhancement at large z or p_{T}. However, the modifications in central Pb+Pb

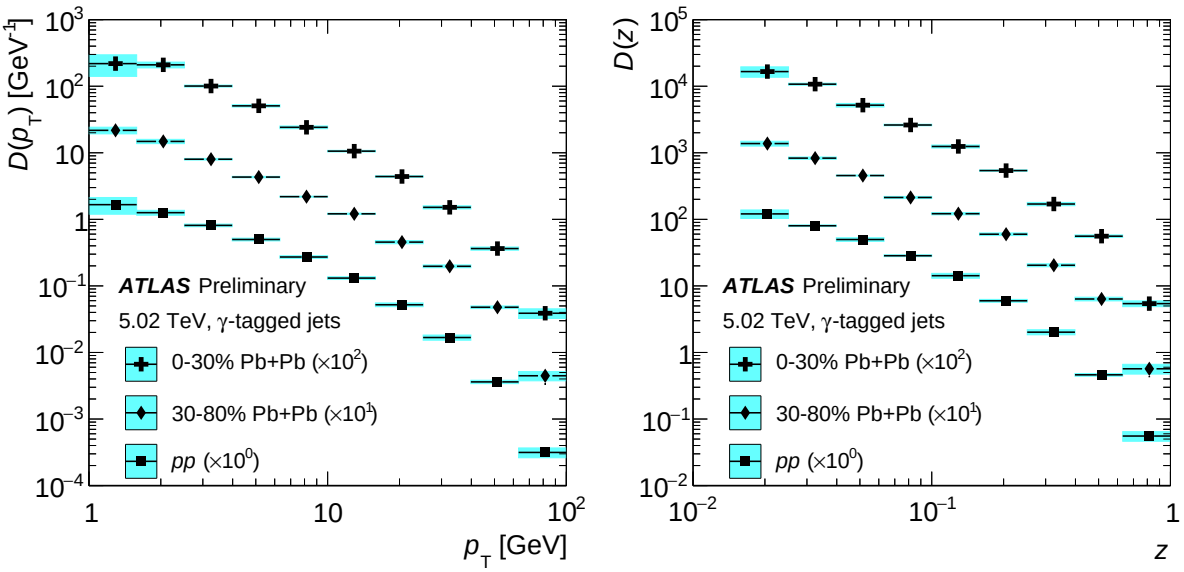

Figure 2: Fragmentation function for jets azimuthally balanced with a high-p_T photon as a function of charged particle p_T (left) or the charged particle p_T to jet p_T ratio z (right). Results are shown for pp collisions and for 30–80% and 0–30% central Pb+Pb collisions. Blue bands show the total systematic uncertainties, while the vertical bars (which are smaller than the marker size in most cases) show the statistical uncertainties.

events appear qualitatively different: the minimum in the Pb+Pb/pp ratio appears shifted to larger z or p_T values, and the large z or p_T region is consistent with no enhancement.

The ratios of the FFs for jets azimuthally balanced with a photon are also compared in Figure 4 to those for inclusively-selected jets in a similar p_T range measured in $\sqrt{s_{NN}} = 2.76$ TeV Pb+Pb and pp collisions [14]. Although the compared measurements are at a different center of mass energy, preliminary results from measurements of inclusive jet FF modification at 5.02 TeV [52] have shown that they are compatible with those at 2.76 TeV within uncertainties. In peripheral collisions, the overall modification pattern for photon-tagged jets is quantitatively similar to that observed for inclusive jets. However, in central collisions, the modifications in the structure of photon-tagged jets are more pronounced, showing an additional relative suppression at high z or p_T, and counter-balancing enhancement at low z or p_T.

As another way to explore the relative change in the FF between different Pb+Pb event classes, the ratio between central and peripheral Pb+Pb collisions is shown in Figure 5. The ratio is consistent with a decreasing linear function of $\log(z)$ or $\log(p_T)$, crossing unity at $z \approx 0.1$ or $p_T \approx 10$ GeV. The analogous ratio is also shown for inclusive jets in Pb+Pb events, which is consistent with unity within uncertainties. Thus, the data indicate that in increasingly central collisions, jets in photon-tagged events are also increasingly modified, in contrast to what is observed for inclusive jets.

7 Conclusion

This note presents a measurement of the charged particle jet fragmentation functions for jets azimuthally balanced with a high-p_T prompt, isolated photon. The measurement is performed in 26 pb^{-1} of pp

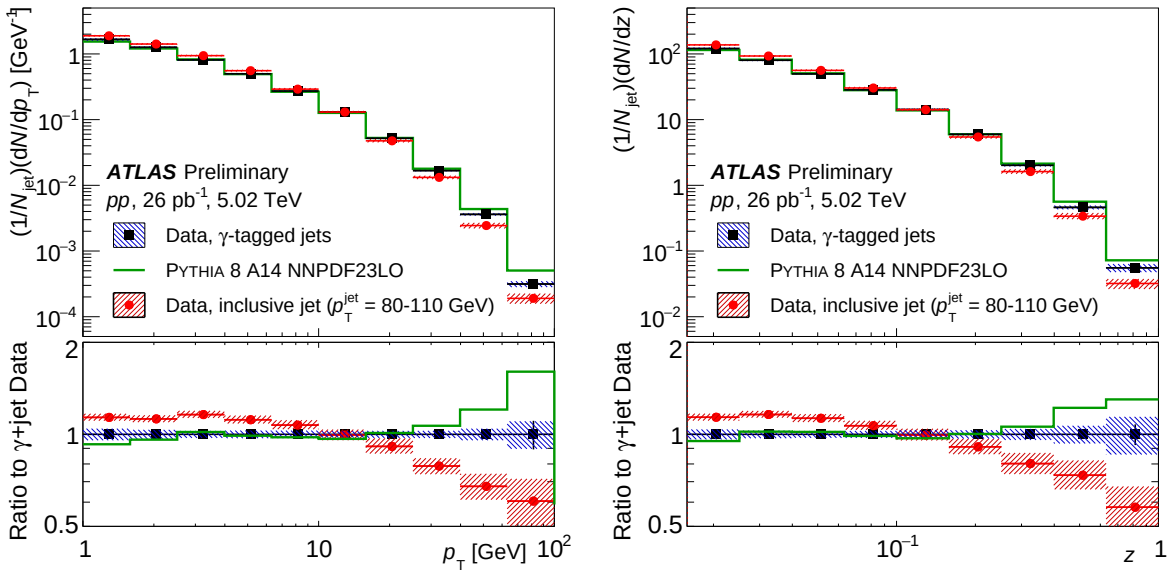

Figure 3: Fragmentation function in pp events as a function of charged particle p_{T} (left) or z (right). Results are shown for the measured distribution for photon-tagged jets (black), the analogous generator-level distribution in PYTHIA 8 events (green), and for the measured distribution for inclusive jets in a similar jet p_{T} range (red). The shaded bands correspond to the total systematic uncertainties on the data.

and 0.49 nb^{-1} of Pb+Pb collision data at $\sqrt{s_{\mathrm{NN}}}$ = 5.02 TeV with the ATLAS detector at the LHC. The kinematic selections are chosen to ensure a topology with a single leading jet with large quark jet fraction for study. In pp collisions, the photon–tagged jet fragmentation functions are systematically harder than those measured in data for inclusive jets, consistent with the expectation based on this flavor difference. Furthermore, they are reasonably well described by event generator simulations. In Pb+Pb collisions, the fragmentation pattern of photon–tagged jets is observed to be modified through interaction with the hot nuclear medium. In 30–80% Pb+Pb events, the modification pattern and overall magnitude is consistent with that for inclusive jets at a similar p_{T} range. However, jets in photon–tagged events are systematically more strongly modified in 0–30% Pb+Pb events, to a degree not observed in inclusive jets. Since previous studies by ATLAS of the rapidity and p_{T}-dependence of fragmentation function modification suggest that the flavor-dependence of such effects is small, these differences may arise in part from the different initial jet p_{T} distributions selected in each analysis. Thus these results raise interesting questions about the interplay of the flavor and kinematic selection of jets with their overall energy loss and modification in high-energy nucleus–nucleus collisions.

References

[1] ATLAS Collaboration, *Measurements of the Nuclear Modification Factor for Jets in Pb+Pb Collisions at* $\sqrt{s_{\mathrm{NN}}}$ = 2.76 *TeV with the ATLAS Detector*, Phys. Rev. Lett. **114** (2015) 072302, arXiv: 1411.2357 [hep-ex].

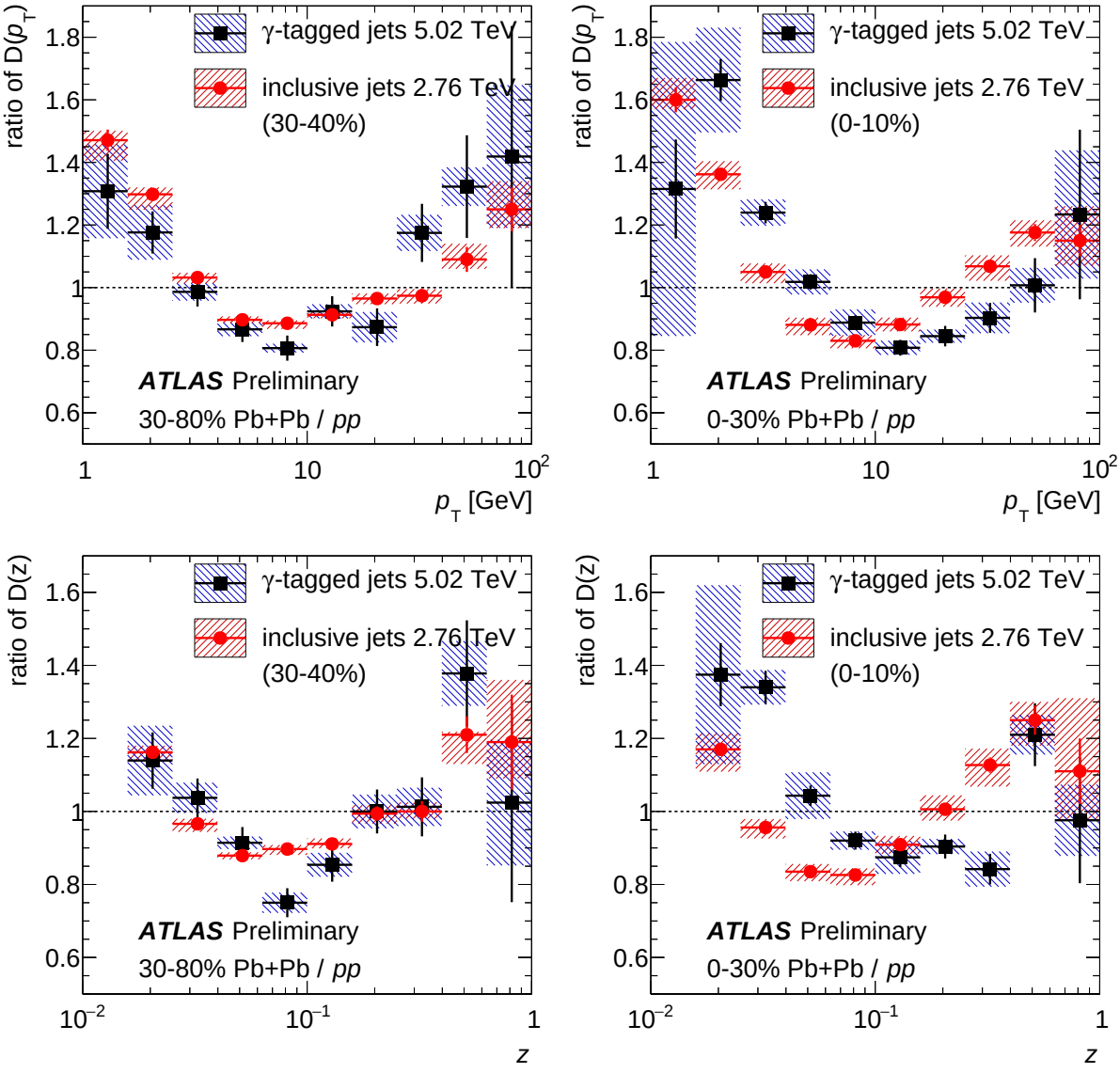

Figure 4: Ratio of the fragmentation function for jets azimuthally balanced with a high-p_{T} photon, between that in 30–80% Pb+Pb collisions and pp collisions (left panels) and 0–30% Pb+Pb collisions and pp collisions (right panels). Results are shown as a function of charged particle p_{T} (top panels) or z (bottom panels), for photon-tagged jets (this measurement, black points) and for inclusive jets in $\sqrt{s_{\mathrm{NN}}}$ = 2.76 TeV Pb+Pb collisions [7, 14] (see text, red points). Hatched bands and vertical bars show the total systematic and statistical uncertainties, respectively, for each measurement.

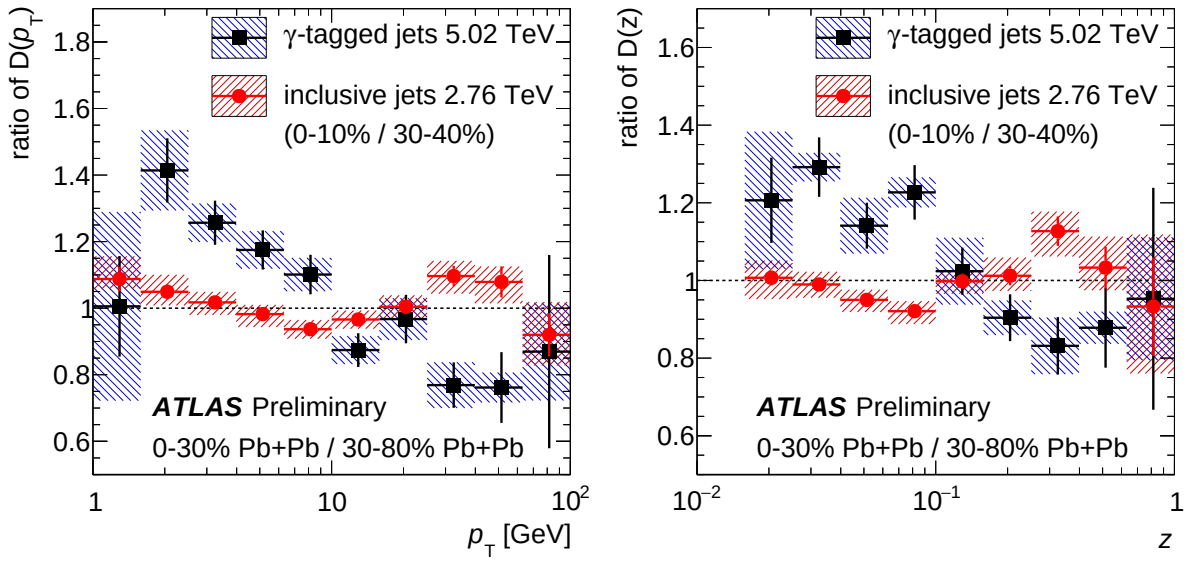

Figure 5: Ratio of the fragmentation function for jets azimuthally balanced with a high-p_T photon, between that in 0–30% Pb+Pb collisions and 30–80% Pb+Pb collisions. Results are shown as a function of charged particle p_T (top panels) or z (bottom panels), for photon-tagged jets (this measurement, black points) and for inclusive jets in $\sqrt{s_{NN}}$ = 2.76 TeV Pb+Pb collisions [7, 14] (see text, red points). Hatched bands and vertical bars show the total systematic and statistical uncertainties, respectively, for each measurement.

[2] ATLAS Collaboration, *Measurement of charged-particle spectra in Pb+Pb collisions at* $\sqrt{s_{NN}}$ = 2.76 *TeV with the ATLAS detector at the LHC*, JHEP **09** (2015) 050, arXiv: 1504.04337 [hep-ex].

[3] ATLAS Collaboration, *Observation of a Centrality-Dependent Dijet Asymmetry in Lead–Lead Collisions at* $\sqrt{s_{NN}}$ = 2.76 *TeV with the ATLAS Detector at the LHC*, Phys. Rev. Lett. **105** (2010) 252303, arXiv: 1011.6182 [hep-ex].

[4] ATLAS Collaboration, *Measurement of jet* p_T *correlations in Pb+Pb and pp collisions at* $\sqrt{s_{NN}}$ = 2.76 *TeV with the ATLAS detector*, (2017), arXiv: 1706.09363 [hep-ex].

[5] ATLAS Collaboration, *Measurement of the jet radius and transverse momentum dependence of inclusive jet suppression in lead–lead collisions at* $\sqrt{s_{NN}}$ = 2.76 *TeV with the ATLAS detector*, Phys. Lett. B **719** (2013) 220, arXiv: 1208.1967 [hep-ex].

[6] CMS Collaboration, *Observation and studies of jet quenching in PbPb collisions at* $\sqrt{s_{NN}}$ = 2.76 *TeV*, Phys. Rev. C **84** (2011) 024906, arXiv: 1102.1957 [hep-ex].

[7] ATLAS Collaboration, *Measurement of inclusive jet charged-particle fragmentation functions in Pb+Pb collisions at* $\sqrt{s_{NN}}$ = 2.76 *TeV with the ATLAS detector*, Phys. Lett. B **739** (2014) 320, arXiv: 1406.2979 [hep-ex].

[8] ATLAS Collaboration, *Measurement of jet fragmentation in* 5.02 *TeV proton-lead and proton-proton collisions with the ATLAS detector*, (2017), arXiv: 1706.02859 [hep-ex].

[9] J. Casalderrey-Solana, D. Gulhan, G. Milhano, D. Pablos and K. Rajagopal, *Angular Structure of Jet Quenching Within a Hybrid Strong/Weak Coupling Model*, JHEP **03** (2017) 135, arXiv: 1609.05842 [hep-ph].

[10] M. Spousta and B. Cole, *Interpreting single jet measurements in Pb + Pb collisions at the LHC*, Eur. Phys. J. **C76** (2016) 50, arXiv: 1504.05169 [hep-ph].

[11] ATLAS Collaboration, *Study of photon-jet momentum correlations in Pb+Pb and pp collisions at* $\sqrt{s_{\mathrm{NN}}} = 5.02$ *TeV with ATLAS*, ATLAS-CONF-2016-110, 2016, URL: https://cds.cern.ch/record/2220772.

[12] CMS Collaboration, *Study of Isolated-Photon + Jet Correlations in PbPb and pp Collisions at* $\sqrt{s_{NN}} = 5.02$ TeV, CMS-PAS-HIN-16-002, 2016, URL: https://cds.cern.ch/record/2217884.

[13] CMS Collaboration, *Study of jet quenching with Z+jet correlations in PbPb and pp collisions at* $\sqrt{s_{\mathrm{NN}}} = 5.02$ *TeV*, (2017), arXiv: 1702.01060 [hep-ex].

[14] ATLAS Collaboration, *Measurement of jet fragmentation in Pb+Pb and pp collisions at* $\sqrt{s_{\mathrm{NN}}} = 2.76$ *TeV with the ATLAS detector at the LHC*, Eur. Phys. J. C **77** (2017) 379, arXiv: 1702.00674 [hep-ex].

[15] CMS Collaboration, *Measurement of jet fragmentation in PbPb and pp collisions at* $\sqrt{s_{\mathrm{NN}}} = 2.76$ *TeV*, Phys. Rev. C **90** (2014) 024908, arXiv: 1406.0932 [hep-ex].

[16] ATLAS Collaboration, *Centrality, rapidity and transverse momentum dependence of isolated prompt photon production in lead–lead collisions at* $\sqrt{s_{\mathrm{NN}}} = 2.76$ *TeV measured with the ATLAS detector*, Phys. Rev. C **93** (2016) 034914, arXiv: 1506.08552 [hep-ex].

[17] L. Adamczyk et al., *Jet-like Correlations with Direct-Photon and Neutral-Pion Triggers at* $\sqrt{s_{NN}} = 200$ *GeV*, Phys. Lett. **B760** (2016) 689, arXiv: 1604.01117 [nucl-ex].

[18] A. Adare et al., *Medium modification of jet fragmentation in Au + Au collisions at* $\sqrt{s_{NN}} = 200$ *GeV measured in direct photon-hadron correlations*, Phys. Rev. Lett. **111** (2013) 032301, arXiv: 1212.3323 [nucl-ex].

[19] J. Casalderrey-Solana, D. C. Gulhan, J. G. Milhano, D. Pablos and K. Rajagopal, *Predictions for Boson-Jet Observables and Fragmentation Function Ratios from a Hybrid Strong/Weak Coupling Model for Jet Quenching*, JHEP **03** (2016) 053, arXiv: 1508.00815 [hep-ph].

[20] Z.-B. Kang, I. Vitev and H. Xing, *Vector boson-tagged jet production in heavy ion collisions at the LHC*, (2017), arXiv: 1702.07276 [hep-ph].

[21] R. Kunnawalkam Elayavalli and K. C. Zapp, *Simulating V+jet processes in heavy ion collisions with JEWEL*, Eur. Phys. J. **C76** (2016) 695, arXiv: 1608.03099 [hep-ph].

[22] J. Casalderrey-Solana, Y. Mehtar-Tani, C. A. Salgado and K. Tywoniuk, *New picture of jet quenching dictated by color coherence*, Phys. Lett. **B725** (2013) 357, arXiv: 1210.7765 [hep-ph].

[23] ATLAS Collaboration, *The ATLAS Experiment at the CERN Large Hadron Collider*, JINST **3** (2008) S08003.

[24] ATLAS Collaboration, *2015 start-up trigger menu and initial performance assessment of the ATLAS trigger using Run-2 data*, ATL-DAQ-PUB-2016-001, 2016, URL: https://cds.cern.ch/record/2136007/.

[25] ATLAS Collaboration, *Measurement of the inclusive isolated prompt photon cross section in pp collisions at* $\sqrt{s} = 8$ *TeV with the ATLAS detector*, JHEP **08** (2016) 005, arXiv: 1605.03495 [hep-ex].

[26] ATLAS Collaboration, *Measurement of the cross section for inclusive isolated-photon production in pp collisions at* $\sqrt{s} = 13$ *TeV using the ATLAS detector*, Phys. Lett. B **770** (2017) 473, arXiv: 1701.06882 [hep-ex].

[27] ATLAS Collaboration, *Measurement of the photon identification efficiencies with the ATLAS detector using LHC Run-1 data*, (2016), arXiv: 1606.01813 [hep-ex].

[28] ATLAS Collaboration, *Electron and photon energy calibration with the ATLAS detector using LHC Run 1 data*, Eur. Phys. J. C **74** (2014) 3071, arXiv: 1407.5063 [hep-ex].

[29] ATLAS Collaboration, *Centrality and rapidity dependence of inclusive jet production in* $\sqrt{s_{\mathrm{NN}}} = 5.02$ *TeV proton-lead collisions with the ATLAS detector*, Phys. Lett. B **748** (2015) 392, arXiv: 1412.4092 [hep-ex].

[30] M. Cacciari, G. P. Salam and G. Soyez, *FastJet User Manual*, Eur. Phys. J. **C72** (2012) 1896, arXiv: 1111.6097 [hep-ph].

[31] ATLAS Collaboration, *Jet Calibration and Systematic Uncertainties for Jets Reconstructed in the ATLAS Detector at* $\sqrt{s} = 13$ *TeV*, ATL-PHYS-PUB-2015-015, 2015, URL: https://cds.cern.ch/record/2037613.

[32] T. Sjostrand, S. Mrenna and P. Z. Skands, *A Brief Introduction to PYTHIA 8.1*, Comput. Phys. Commun. **178** (2008) 852, arXiv: 0710.3820 [hep-ph].

[33] R. D. Ball et al., *Parton distributions with LHC data*, Nucl. Phys. **B867** (2013) 244, arXiv: 1207.1303 [hep-ph].

[34] ATLAS Collaboration, *ATLAS Pythia 8 tunes to 7 TeV data*, ATL-PHYS-PUB-2014-021, 2014, URL: https://cds.cern.ch/record/1966419.

[35] S. Agostinelli et al., *GEANT4: A Simulation toolkit*, Nucl. Instrum. Meth. **A506** (2003) 250.

[36] ATLAS Collaboration, *The ATLAS Simulation Infrastructure*, Eur. Phys. J. C **70** (2010) 823, arXiv: 1005.4568 [hep-ex].

[37] T. Gleisberg et al., *Event generation with SHERPA 1.1*, JHEP **02** (2009) 007, arXiv: 0811.4622 [hep-ph].

[38] H.-L. Lai et al., *New parton distributions for collider physics*, Phys. Rev. **D82** (2010) 074024, arXiv: 1007.2241 [hep-ph].

[39] J. Bellm et al., *Herwig 7.0/Herwig++ 3.0 release note*, Eur. Phys. J. **C76** (2016) 196, arXiv: 1512.01178 [hep-ph].

[40] L. A. Harland-Lang, A. D. Martin, P. Motylinski and R. S. Thorne, *Parton distributions in the LHC era: MMHT 2014 PDFs*, Eur. Phys. J. **C75** (2015) 204, arXiv: 1412.3989 [hep-ph].

[41] ATLAS Collaboration,
Jet energy measurement with the ATLAS detector in proton–proton collisions at $\sqrt{s} = 7$ *TeV*,
Eur. Phys. J. C **73** (2013) 2304, arXiv: 1112.6426 [hep-ex].

[42] ATLAS Collaboration, *High-E_{T} isolated-photon plus jets production in pp collisions at* $\sqrt{s} = 8$ *TeV with the ATLAS detector*, Nucl. Phys. B **918** (2017) 257,
arXiv: 1611.06586 [hep-ex].

[43] G. D'Agostini, *A Multidimensional unfolding method based on Bayes' theorem*,
Nucl. Instrum. Meth. **A362** (1995) 487.

[44] T. Adye, 'Unfolding algorithms and tests using RooUnfold',
Proceedings, PHYSTAT 2011 Workshop on Statistical Issues Related to Discovery Claims in Search Experiments and Unfolding, CERN,Geneva, Switzerland 17-20 January 2011,
CERN, CERN, 2011 313, arXiv: 1105.1160 [physics.data-an],
URL: https://inspirehep.net/record/898599/files/arXiv:1105.1160.pdf.

[45] ATLAS Collaboration,
Jet energy scale and its uncertainty for jets reconstructed using the ATLAS heavy ion jet algorithm,
ATLAS-CONF-2015-016, 2015, URL: https://cds.cern.ch/record/2008677.

[46] ATLAS Collaboration, *Jet energy measurement and its systematic uncertainty in proton–proton collisions at* $\sqrt{s} = 7$ *TeV with the ATLAS detector*, Eur. Phys. J. C **75** (2015) 17,
arXiv: 1406.0076 [hep-ex].

[47] ATLAS Collaboration,
Early Inner Detector Tracking Performance in the 2015 Data at $\sqrt{s} = 13$ *TeV*,
ATL-PHYS-PUB-2015-051, 2015, URL: https://cds.cern.ch/record/2110140.

[48] ATLAS Collaboration, *Measurement of track reconstruction inefficiencies in the core of jets via pixel dE/dx with the ATLAS experiment using* $\sqrt{s} = 13$ *TeV pp collision data*,
ATL-PHYS-PUB-2016-007, 2016, URL: https://cds.cern.ch/record/2140460.

[49] R. Akers et al.,
A Model independent measurement of quark and gluon jet properties and differences,
Z. Phys. **C68** (1995) 179.

[50] R. Barate et al., *Measurements of the structure of quark and gluon jets in hadronic Z decays*,
Eur. Phys. J. **C17** (2000) 1.

[51] G. Abbiendi et al., *Experimental properties of gluon and quark jets from a point source*,
Eur. Phys. J. **C11** (1999) 217, arXiv: hep-ex/9903027 [hep-ex].

[52] ATLAS Collaboration, *Measurement of jet fragmentation in* 5.02 *TeV lead–lead and proton–proton collisions with the ATLAS detector*, ATLAS-CONF-2017-005, 2017,
URL: https://cds.cern.ch/record/2244802.

Appendix

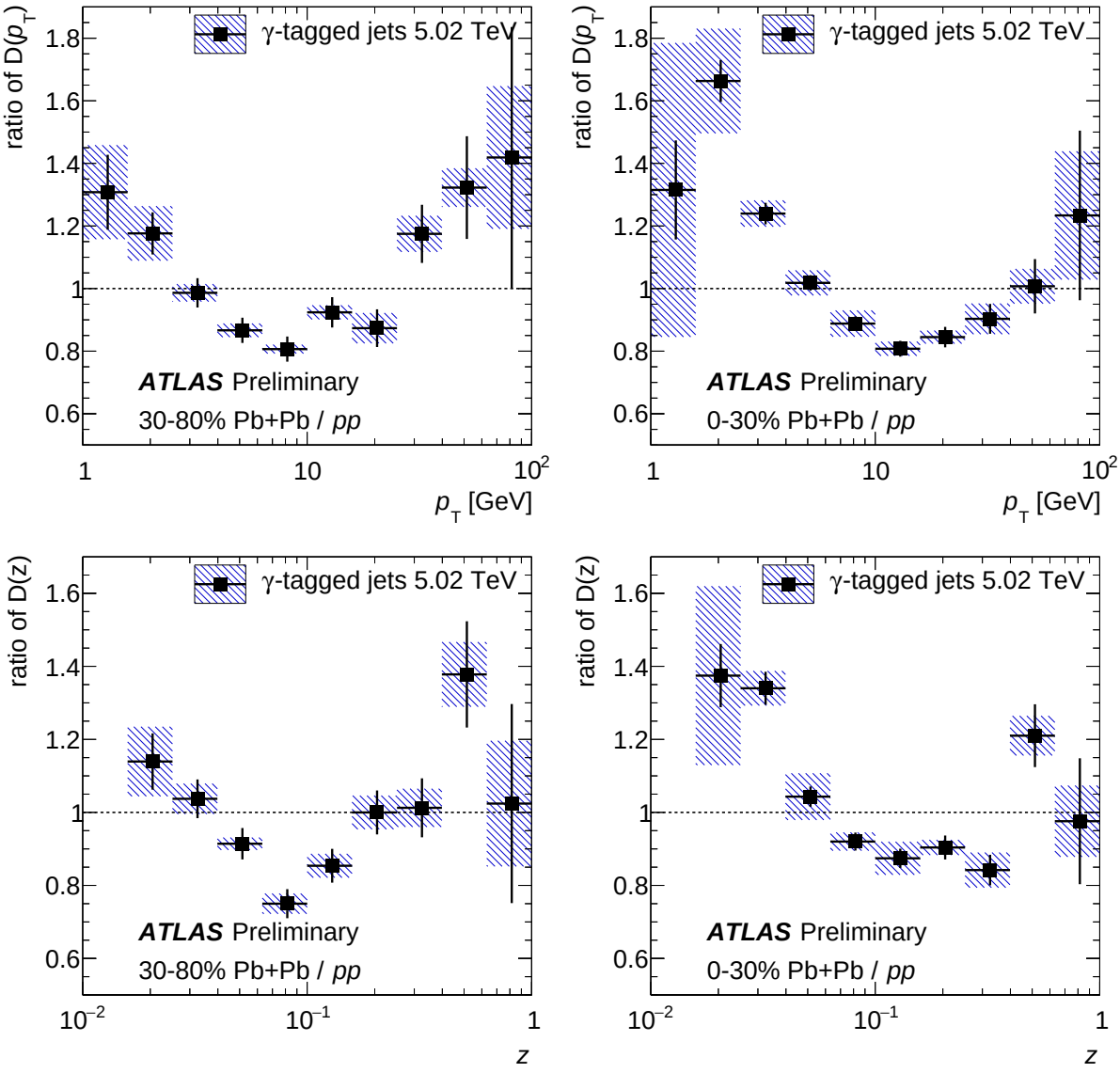

Figure 6: Ratio of the fragmentation function for jets azimuthally balanced with a high-p_{T} photon, between that in 30–80% Pb+Pb collisions and pp collisions (left panels) and 0–30% Pb+Pb collisions and pp collisions (right panels). Results are shown as a function of charged particle p_{T} (top panels) or z (bottom panels). Hatched bands and vertical bars show the total systematic and statistical uncertainties, respectively, for each measurement.

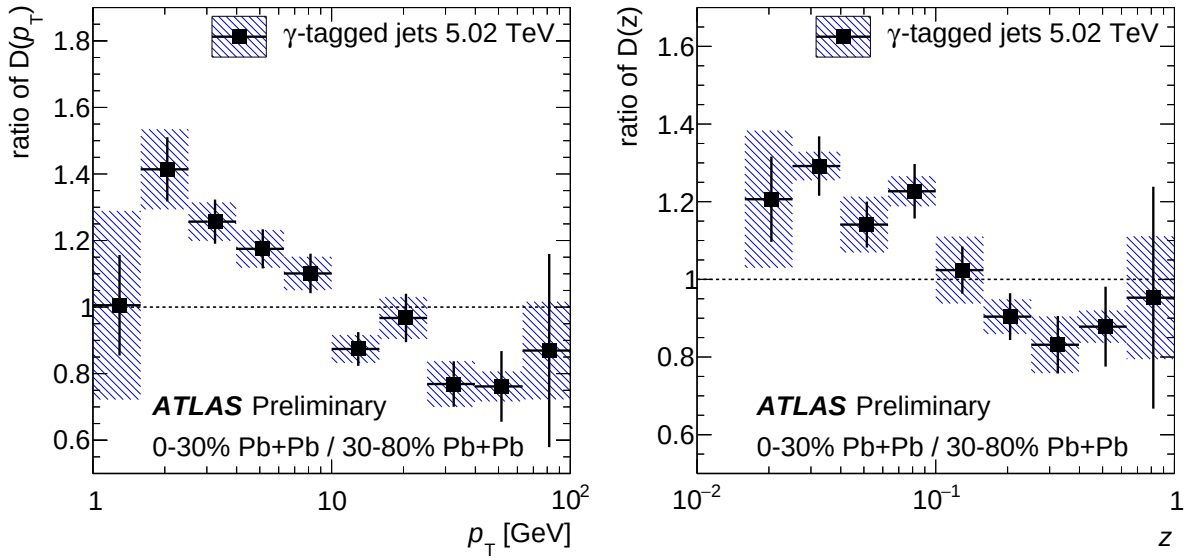

Figure 7: Ratio of the fragmentation function for jets azimuthally balanced with a high-p_T photon, between that in 0–30% Pb+Pb collisions and 30–80% Pb+Pb collisions. Results are shown as a function of charged particle p_T (top panels) or z (bottom panels). Hatched bands and vertical bars show the total systematic and statistical uncertainties, respectively, for each measurement.